Soft Matter

PAPER

View Article Online
View Journal | View Issue

Cite this: *Soft Matter*, 2025, **21**, 7508

Signatures of polar order in a ferroelectric nematic liquid crystal: splay stiffening and twist softening

Evangelia E. Zavvou, *[ab] Alexander Jarosik, [b] Hajnalka Nádasi, [b] Christoforos A. Krontiras,[a] Panagiota K. Karahaliou, [a] Rachel P. Tuffin, [c] Melanie Klasen-Memmer [c] and Alexey Eremin *[a]

Received 27th June 2025,
Accepted 2nd September 2025

DOI: 10.1039/d5sm00670h

rsc.li/soft-matter-journal

The recent discovery of ferroelectric nematics—genuine 3D ferroelectric fluids—has underscored the importance of electrostatic interactions in shaping the physical behaviour of soft matter systems. In this paper, we investigate the mechanical properties of ferroelectric nematics by directly comparing the splay and twist elastic constants in a liquid crystal system that exhibits both nonpolar and ferroelectric nematic phases. Our results reveal that polar ordering results in increased splay rigidity and a concomitant reduction in twist elasticity.

1. Introduction

Uniaxial nematic liquid crystals constitute the simplest and most widely studied class of liquid crystalline phases due to their fundamental importance and diverse applications.[1] The nematic phase (N) is characterised by long-range orientational order, with molecules aligning on average along a common axis, defined by the nematic director **n**. However, the symmetry of conventional nematics is not polar but cylindrical, as reflected in the invariance of the director under inversion ($\mathbf{n} \rightarrow -\mathbf{n}$). This symmetry fundamentally dictates the mechanical properties of nematics, particularly their response to director deformations.

A unique property of liquid crystals is their ability to transmit torques through deformations of the director field.[1] In 1927, Fréedericksz demonstrated that when a nematic liquid crystal confined between two parallel plates is exposed to external electric or magnetic field, the director reorientation—known as the Fréedericksz transition—exhibits a threshold behaviour.[2] By analysing changes in optical transmittance or capacitance during this transition, one can determine the nematic elastic constants.[1]

Nematic phases with vector symmetries have recently been identified in both ferromagnetic[3,4] and ferroelectric systems.[5–9] The prototypical representatives of the ferroelectric nematic phase (N_F) are RM734[6] and DIO,[5] strongly polar, low-molecular-mass mesogens with wedge-like molecular geometries and multiple dipolar groups. These features result in an overall longitudinal dipole moment on the order of 10 D, along with strong optical nonlinearity and an exceptionally high dielectric permittivity in thin-film cells.[8,10] The precise nature of this dielectric response remains an active area of research, with the polarisation capacitance goldstone (PCG) mode and continuous phenomenological model (CPM) being among the leading theoretical frameworks under experimental investigation.[11–14]

Research on ferroelectric nematics is driven by their potential applications in fast electrooptical and electromechanical devices. The mechanoelectrical effect in the N_F phase[15] opens new possibilities for sensor and touch applications, as well as tunable optical filters. Additionally, their strong optical nonlinearity makes N_F materials promising candidates for photonic devices and communication technologies.

Over the past few years, intensive research efforts have led to a rapid expansion of the catalogue of mesogens capable of forming the N_F phase. Alongside these developments, there has been substantial progress in characterizing the N–N_F and N–M–N_F phase transitions, where M denotes an intermediate antiferroelectric phase.[16,17] This phase has been proposed to correspond to the antiferroelectric SmZ_A phase, in which the nematic director is oriented perpendicular to the layer normal, leading to distinct structural and dielectric properties.[18] Antiferroelectric order in this phase can be manipulated by the addition of ionic liquids as demonstrated by Rupnik *et al.*[19]

Polar heliconical phases have also been discovered, in which the helical pitch can be controlled by small electric fields.[20–22] This allows for tuning of the selective reflection in the visible range.

[a] *Department of Physics, University of Patras, Patras, 26504, Greece. E-mail: ezavvou@upatras.gr*
[b] *Otto von Guericke University Magdeburg, Institute of Physics, Dept. Nonlinear Phenomena, Magdeburg, 39106, Germany. E-mail: alexey.eremin@ovgu.de*
[c] *Merck Electronics KGaA, 250 Frankfurter Str., D-64293 Darmstadt, Germany*

The coupling between the spontaneous electric polarisation and the nematic director results in an electrostatic contribution to the director's deformation energy, significantly affecting the material's mechanical properties. The avoidance of the polarisation charges resulting from the divergence of the director stiffens the splay elasticity of the N_F phase.[9,23–26] Such stiffening is reflected in the formation of conics in thin N_F films on a glycerine surface and also in the drastic increase of the threshold of the magnetic Fréederiksz transition reported for the N_F compounds.[23,26] In our previous paper, we reported on the measurements of the splay and the twist elastic constants in a compound exhibiting a direct isotropic-N_F phase transition.[26]

We demonstrated that the ferroelectric N_F phase is much less susceptible to splay deformation than to twist, as evidenced by the pronounced increase in the threshold of the magnetic splay Fréedericksz transition compared with conventional nematics; however, a direct comparison with the mechanical behaviour of the paraelectric N phase was not possible in that study, as the compound did not exhibit a nematic phase. The enhanced splay rigidity of the N_F phase is attributed to the electrostatic self-interaction of spontaneous polarisation, which suppresses polarisation splay, although our model indicates that this stiffening is mitigated by ionic screening.

In this paper, we explore the mechanical, dielectric and nonlinear optical properties of a liquid crystalline mixture exhibiting the intermediate antiferroelectric phase in between the nematic and the ferroelectric nematic phases, with the latter being stable at and below room temperature. We directly compare the elastic constants of the nonpolar N and the polar N_F phases through the analysis of the capacitance and/or optical transmission recorded during the Fréedericksz transition. The temperature dependence of the diamagnetic anisotropy in the N phase is determined through complementary studies in external electric and magnetic fields. To avoid the undesired electric field effects, the mechanical properties within the N_F phase are explored through measurements of the optical transmission in an external magnetic field.

2. Experimental

The studied material, MDA-21-671 (provided by Merck Electronics KGaA, Darmstadt, Germany), is a mixture exhibiting the following phase sequence: crystal < -20 °C $\rightarrow$ N_F 45.8 °C $\rightarrow$ M 57.9 °C $\rightarrow$ N 87.6 °C $\rightarrow$ isotropic. The coexistence range of the nematic and isotropic phases is narrow, not exceeding 2 °C.[27]

Phase identification and birefringence measurements were carried out using an AxioImager A.1 polarising optical microscope (Carl Zeiss, GmbH, Germany) equipped with a heating stage (Instec, USA) and a Berek tilting compensator. The material was filled into a planar-aligned cell (E.H.C., Japan) with a 6 μm gap and parallel rubbing. Measurements were taken upon cooling from the isotropic phase using monochromatic light with wavelength λ = 546 nm.

The presence of polar order in the liquid crystalline phases of the studied compound was confirmed *via* optical second harmonic generation (SHG) measurements using a Nd:YAG laser. The fundamental beam had a wavelength of λ = 1064 nm, a pulse width of 10 ns, and a repetition rate of 10 Hz. The sample was introduced into custom-made in-plane-switching (IPS) cells with planar alignment and a thickness of 10 μm. The incident beam struck the sample at an angle of 30° to the cell normal. The SHG signal was collected in transmission using a photomultiplier tube (Hamamatsu) and calibrated against a 10 μm reference quartz plate. Measurements were carried out upon cooling from the isotropic phase in 1 °C increments.

Fluorescence and SHG microscopy studies were performed using a multiphoton (MP) confocal microscope (Leica TCS SP8) with excitation at the fundamental wavelength λ = 880 nm. For fluorescence imaging, samples were doped with 0.01 wt% of the dichroic dye *N*,*N*′-bis(2,5-di-*tert*-butylphenyl)-3,4,9,10-perylenedicarboximide (BTBP, Sigma-Aldrich) to visualise the director orientation. Excitation was performed using a laser source at λ_{ex} = 488 nm.

The complex dielectric permittivity, $\varepsilon^*(\omega) = \varepsilon'(\omega) - i\varepsilon''(\omega)$, in the isotropic and liquid crystalline phases of the studied mixture was measured over the frequency range from 0.1 Hz to 1 GHz. This was achieved by combining a Novocontrol Alpha-N Frequency Response Analyser (f = 0.1 Hz–1 MHz) for the low-frequency regime and an HP4291B RF Impedance Analyser (f = 1 MHz–1 GHz) for the high-frequency range.

The sample was sandwiched between two untreated, gold-plated brass electrodes (5 mm diameter), separated by 50 μm-thick silica fibres. For low-frequency measurements, the cell was mounted in a modified BDS1200 sample holder; in the high-frequency regime, a BDS2200 RF sample cell was used, placed at the end of a coaxial line (Novocontrol). In both cases, the sample cell was housed in a Novocontrol cryostat, with temperature precisely controlled and stabilised to within ±0.02 °C using a Quatro Cryosystem (Novocontrol).

Isothermal frequency scans were recorded upon slow cooling from the isotropic phase at a rate of 0.25 °C min^{-1}, with variable temperature steps. The oscillating voltage was set to U_{rms} = 0.01 V. Data acquisition and storage were managed *via* WinDETA software (Novocontrol).

The resulting dielectric spectra were analysed using the Havriliak–Negami (HN) equation:

$$\varepsilon^*(\omega) = \varepsilon_\infty + \sum_\kappa \frac{\Delta\varepsilon_\kappa}{\left(1 + (i\omega\tau_{HN,\kappa})^{\alpha_\kappa}\right)^{\beta_\kappa}} + \frac{\sigma_{DC}}{i\omega\varepsilon_0}, \qquad (1)$$

where ε_∞ is the high-frequency permittivity, $\Delta\varepsilon_\kappa$ denotes the dielectric strength of the corresponding relaxation process, σ_{DC} is the DC conductivity. The characteristic relaxation time $\tau_{HN,\kappa}$ is related to the frequency of maximum dielectric loss *via*:

$$f_{max,\kappa} = \frac{1}{2\pi\tau_{HN,\kappa}}\left[\sin\left(\frac{\pi\alpha_\kappa}{2+2\beta_\kappa}\right)\right]^{\frac{1}{\alpha_\kappa}}\left[\sin\left(\frac{\pi\alpha_\kappa\beta_\kappa}{2+2\beta_\kappa}\right)\right]^{-\frac{1}{\alpha_\kappa}}, \qquad (2)$$

The shape parameters α_κ and β_κ characterise the symmetric and asymmetric broadening of the relaxation time distribution, respectively, and satisfy the condition $0 < \alpha_\kappa, \alpha_\kappa\beta_\kappa \leq 1$.

When $\alpha_\kappa = \beta_\kappa = 1$, eqn (1) reduces to the Debye equation. Deconvolution of the dielectric spectra was performed using the WinFit software (Novocontrol).

The mechanical and magnetooptical properties were evaluated through complementary magnetic and electric Fréedericksz transition (FT) experiments. In both cases, the material was filled into planar cells (E.H.C., Japan) with a thickness of 25 μm, equipped with parallel rubbing alignment layers and ITO electrodes with a sheet resistance of 10 Ω.

For the electric Fréedericksz transition, the cell capacitance was measured as a function of the applied alternating voltage (U_{rms} = 0.01–3 V) using an Alpha-N analyser (Novocontrol). A time interval of 30 s was maintained between the application of the electric field and the capacitance measurement. The frequency of the applied AC field (f = 0.7–5 kHz) was carefully optimised at each temperature to minimise low-frequency ionic effects, while ensuring the measurement remained within the quasi-static dielectric regime. To achieve an undistorted initial director configuration, the sample was heated to the isotropic phase between successive FT measurements and then slowly cooled to the target temperature.

The measured dielectric permittivity as a function of applied AC voltage, $\varepsilon_{EQ}(U)$, was interpreted as the effective permittivity of a series capacitor network consisting of three layers: two polyimide (PI) alignment layers with capacitance $C_{PI} = \varepsilon_{PI}\varepsilon_0 A/d_{PI}$, and the liquid crystal (LC) layer with capacitance $C_{LC} = \varepsilon_{LC}\varepsilon_0 A/d$. Here, A is the electrode area, d and d_{PI} are the thicknesses of the LC and PI layers, respectively. The empty cell capacitance was defined as $C_0 = \varepsilon_0 A/d$ and was measured prior to sample filling. The dielectric permittivity of the LC layer, $\varepsilon_{LC}(U)$, was recalculated from the measured $\varepsilon_{EQ}(U)$ using the relation: $\varepsilon_{LC} = \varepsilon_{EQ}\varepsilon_{PI}/[\varepsilon_{PI} - 2\varepsilon_{EQ}(d_{PI}/d)]$. In this calculation, the PI layer thickness was assumed to be d_{PI} = 20 nm (LX-1400 polyimide by Hitachi), and the permittivity of the polyimide was taken as ε_{PI} = 3.5, a typical value that is expected to be nearly temperature- and frequency-independent.

The dielectric anisotropy and the splay (K_{11}) and bend (K_{33}) elastic constants were determined in the high-temperature nematic phase by fitting the recalculated $\varepsilon_{LC}(U)$ curves using the expressions:[28]

$$U = \frac{2U_{th}}{\pi}\sqrt{1+\gamma\sin^2\theta_m} \times \int_0^{\pi/2}\left[\frac{1+\kappa\sin^2\theta_m\sin^2\psi}{(1+\gamma\sin^2\theta_m\sin^2\psi)(1-\sin^2\theta_m\sin^2\psi)}\right]^{1/2} d\psi, \quad (3)$$

and

$$\varepsilon = \varepsilon_\perp \frac{\int_0^{\pi/2}\left[\frac{(1+\gamma\sin^2\theta_m\sin^2\psi)(1+\kappa\sin^2\theta_m\sin^2\psi)}{(1-\sin^2\theta_m\sin^2\psi)}\right]^{1/2} d\psi}{\int_0^{\pi/2}\left[\frac{1+\kappa\sin^2\theta_m\sin^2\psi}{(1+\gamma\sin^2\theta_m\sin^2\psi)(1-\sin^2\theta_m\sin^2\psi)}\right]^{1/2} d\psi}, \quad (4)$$

where, θ_m is the director deflection angle in the mid-plane, $\kappa = (K_{33} - K_{11})/K_{11}$ and $\gamma = (\varepsilon_\parallel - \varepsilon_\perp)/\varepsilon_\perp$. Data fitting was implemented in Matlab using a nonlinear optimisation solver to minimise a cost function defined on the experimental dataset. Interpolation was used to obtain the function values at the experimental points. The fitting parameters were U_{th}, κ and γ. The perpendicular component of the dielectric permittivity $\varepsilon_\perp$ was deduced from the recalculated sample capacitance well below the onset of the Fréedericksz transition.

For the magnetic Fréedericksz transition, 25 μm -thick planar cells filled with the material were placed between a pair of Helmholtz coils capable of generating magnetic flux densities up to 650 mT. The magnetic field–induced splay and twist Fréedericksz transitions enabled the determination of the corresponding elastic constants, K_{11} and K_{22}, through the evaluation of the corresponding critical magnetic field strengths at the onset of the splay/twist Fréedericksz transition, by monitoring the optical transmission of the sample between crossed polarising prisms (Thorlabs) as a function of the applied magnetic field.[26] The diamagnetic anisotropy in the N phase was determined through the combination of results of Fréedericksz transition in electric and magnetic fields, as discussed later in the text.

The sample was illuminated using a He–Ne laser. The rubbing direction of the cell was oriented perpendicular to the magnetic field and at an angle of 45° with respect to the crossed polarisers to maximize birefringence sensitivity.

In the splay geometry, the magnetic field was applied perpendicular to the cell plane; in the twist configuration, it was applied parallel to the cell plane. All measurements were carried out upon cooling from the isotropic phase.

3. Results and discussion

3.1. Optical characterisation

Polarising optical microscopy (POM) observations and birefringence measurements were performed using commercial planar cells with parallel rubbing and a spacing of 6 μm. Upon cooling from the isotropic liquid, a uniformly aligned nematic phase emerged, as shown in Fig. 1a.

The transition to the intermediate M phase was accompanied by a progressive suppression of director fluctuations (flickering), along with the development of a grainy texture (Fig. 1b). Further cooling led to the formation of the N_F phase, characterised by the appearance of a striped texture, with stripes oriented parallel to the rubbing direction. These observations are consistent with previously reported studies of the mesogen DIO, which exhibits the same phase sequence as the studied mixture.[5,29]

At lower temperatures, line defects were observed (Fig. 1c), which subsequently annihilated, giving rise to a uniformly aligned N_F phase. This alignment is promoted by the parallel rubbing of the top and bottom glass substrates.[30]

The temperature dependence of birefringence, measured upon cooling from the isotropic liquid, is shown in Fig. 2.

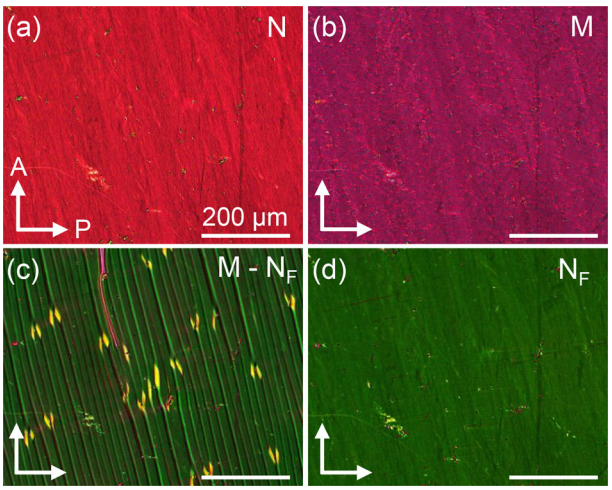

Fig. 1 Polarising optical microscopy textures of the studied compound in a 6 μm thick planar cell with parallel rubbing: (a) N phase at 60 °C, (b) M phase at 46.4 °C, (c) N_F phase at 38.8 °C and (d) N_F phase at 28 °C. The rubbing direction forms an angle of 15° with the analyser. The white bar is 200 μm.

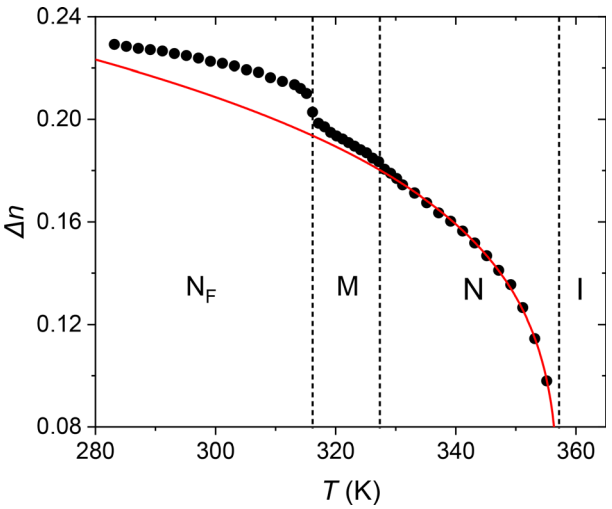

Fig. 2 Temperature dependence of birefringence (Δn) in the liquid crystalline phases of the studied material determined at λ = 545 nm. Black circles correspond to experimental data, while the solid line represents the theoretical fitting according to eqn (5).

Within the nematic phase, the birefringence increases on cooling and follows a Haller-like temperature dependence:[31]

$$\Delta n = \Delta n_0 \left(1 - \frac{T}{T^*_{IN}}\right)^{\beta} \quad (5)$$

where Δn_0 is the extrapolated birefringence at T = 0 K, T^*_{IN} is a fitting parameter slightly above the isotropic–nematic transition temperature, and β is a critical exponent. The best-fit parameters are $\Delta n_0 = 0.315 \pm 0.005$, $T^*_{IN} = (357.2 \pm 0.3)$ K, and $\beta = 0.225 \pm 0.006$.

The orientational order parameter, defined as $S = \Delta n/\Delta n_0$, reaches values around $S \approx 0.57$ near the N–M phase transition.

Notably, both the Haller-like behaviour of Δn in the high-temperature N phase and the small value of $\beta \sim 0.2$ are characteristic of conventional nematogens, as observed in other ferroelectric liquid crystals.[9,10,32]

Upon entering the intermediate M phase, birefringence progressively deviates from the Haller trend, increasing above the expected values. A distinct jump in Δn is observed at the M–N_F transition, followed by a gradual increase within the N_F phase. These findings are consistent with the weakly first-order character of the M–N_F transition,[5,10] and they further support an increase in orientational order associated with the emergence of long-range polar order in the N_F phase.

3.2. Nonlinear optical response

To investigate the polar nature of the N_F phase, we performed second harmonic generation (SHG) measurements. A strong, spontaneous SHG signal emerges as the system transitions into the N_F phase, with its intensity exhibiting a pronounced temperature dependence (Fig. 3a). In planar cells with parallel rubbing, which ensures uniform director alignment, SHG efficiency reaches a maximum when the polarisation of the incident beam is parallel to the nematic director (see inset in Fig. 3a). A similar response was observed in thin films of the N_F phase prepared on untreated substrates.

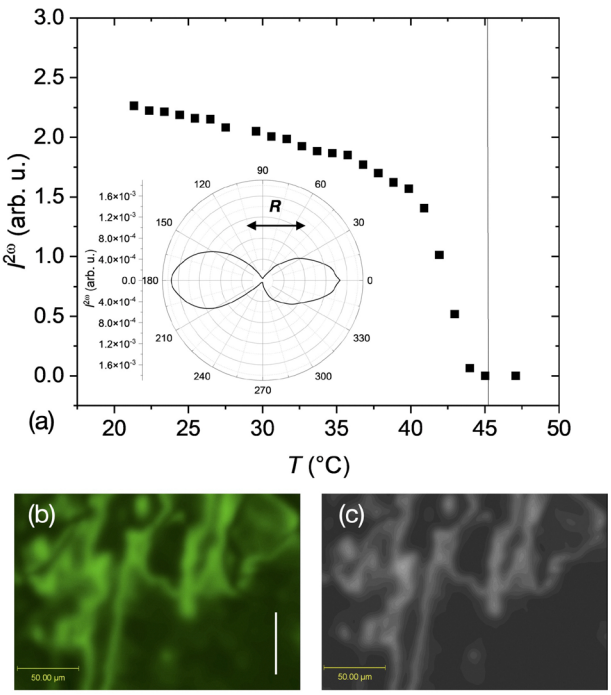

Fig. 3 Second Harmonic Generation: (a) temperature dependence of the $I^{2\omega}(T)$ of a sample confined in a cell with planar director anchoring. The inset shows the dependence of the SHG signal on the angle between the alignment direction **R** and the polarisation plane of the probing laser (T = 21 °C). (b) Fluorescence microscopy image of a sample with untreated substrates and (c) the corresponding SHG microscopy image. The images are taken at T = 21 °C and the bar indicates the polarisation state of the probing laser.

For direct visualisation of the director field, we employed the dichroic dye BTBP, which preferentially absorbs light polarised along the nematic director. Fig. 3b shows the fluorescence pattern in a thin section of the sample, while Fig. 3c presents the corresponding SHG microscopy image of the same region. The close similarity between the fluorescence and SHG textures confirms the parallel alignment of the nematic polar directors.

3.3. Dielectric properties

Dielectric spectroscopy (DS) was employed to investigate the polarisation dynamics across the isotropic and liquid crystalline phases of the studied compound. DS is a powerful technique for probing the relaxation of dipolar correlations and the emergence of collective dipolar motions, making it an indispensable tool for the characterisation of ferroelectric nematogens.

The dielectric response was recorded over a wide frequency range (0.1 Hz–1 GHz) and is presented in Fig. 4 as a three-dimensional plot of the imaginary part of the dielectric permittivity (ε'') as a function of temperature and frequency. In the isotropic phase, a single relaxation process is observed, with the frequency of maximum dielectric loss, f_{max}, located around 10^7 Hz. Upon cooling into the nematic phase, a relaxation process emerges at lower f_{max}, accompanied by a notable increase in dielectric strength. This finding indicates that the untreated gold-plated electrodes promote spontaneous homeotropic alignment of the nematic director, thereby enabling the measurement of the dielectric permittivity component parallel to the director. This behaviour is consistent with previous reports on prototypical ferroelectric nematogens, such as RM734 and DIO, where a strong tendency for out-of-plane director alignment was also observed in similar sample cells with untreated gold-plated electrodes.[8,14,33] Although the director alignment is implicitly determined through measurements with untreated gold electrodes, this configuration eliminates the contribution of the large capacitance of the polymer aligning layers in series with the LC sample. However, thin interfacial layers of the LC itself can form near the electrodes and should be taken into account when interpreting the dielectric response within the N_F phase.[10–13,34]

The deconvolution of the dielectric spectra was performed by simultaneously fitting the real, $\varepsilon'(\omega)$, and imaginary, $\varepsilon''(\omega)$, components of the dielectric permittivity using eqn (1). Representative examples of the deconvoluted spectra for the studied material are shown in Fig. S1. The temperature dependence of the relaxation frequency maxima (f_{max}) and the corresponding dielectric strengths ($\Delta\varepsilon$) for each fitted relaxation mode are presented in Fig. 5a and b, respectively.

In the isotropic phase, the spectra were well described by a single relaxation mode (m_{iso}) of Havriliak–Negami type, with a maximum loss frequency on the order of 10^7 Hz and a dielectric strength of approximately $\Delta\varepsilon_{m,iso} \approx 40$. This relaxation process is attributed to the overall reorientational motions of dipolar units in the isotropic environment and follows an Arrhenius temperature dependence:

$$f_{max}(T) = f_0 \exp\left(-\frac{E_A}{k_B T}\right),$$

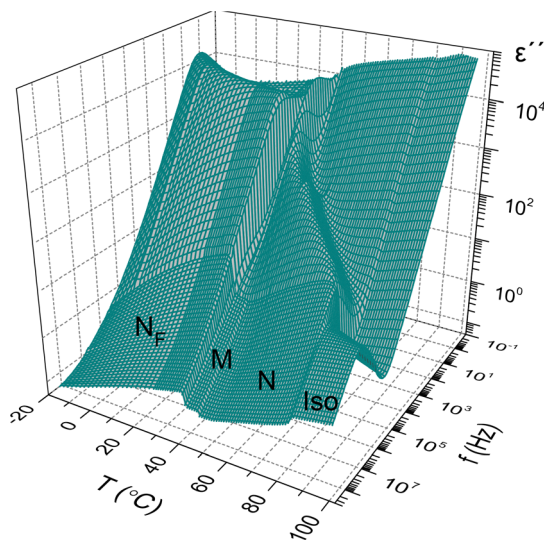

Fig. 4 3D plot of the imaginary part of the complex dielectric permittivity (ε'') as a function of temperature and frequency measured in 50 μm thick parallel plate capacitor with untreated gold-plated brass electrodes.

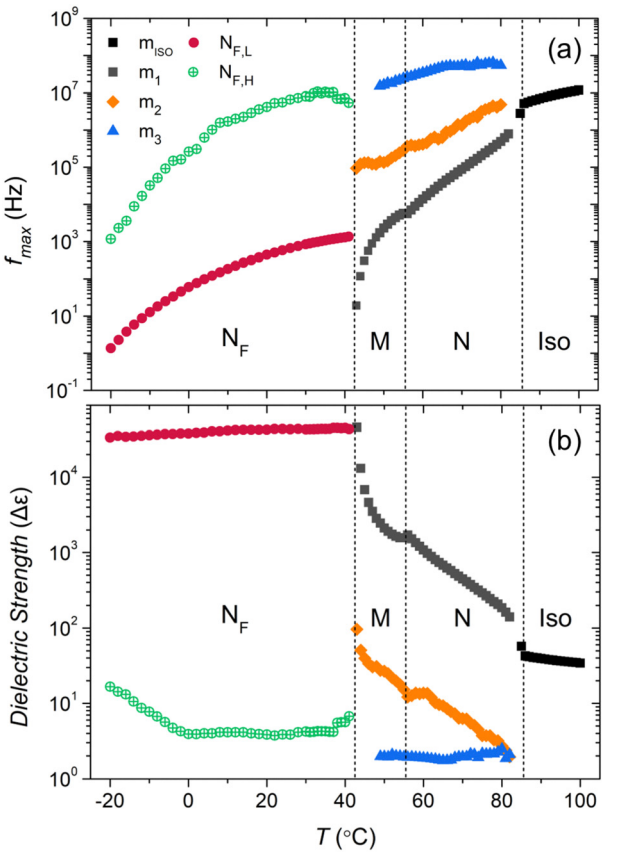

Fig. 5 (a) Temperature dependence of the relaxation frequency maxima (f_{max}) and (b) the dielectric strengths ($\Delta\varepsilon$) of the recorded relaxation mechanisms, obtained through fitting of the dielectric spectra with eqn (1).

with an activation energy $E_A \approx 65$ kJ mol^{-1}, consistent with values reported for conventional nematogens.[35]

In the N and M phases, three distinct relaxation mechanisms are identified, denoted m_1, m_2, and m_3 in order of increasing relaxation frequency (Fig. 5a). The most prominent in terms of dielectric strength is the m_1 mode, which exhibits a nearly Debye-like character, with $\alpha_1 \approx 0.97$. The intermediate-frequency mode m_2 also displays a close-to-Debye shape, featuring symmetric broadening of the relaxation time distribution ($\alpha_2 \approx 0.9$–0.7). In contrast, the high-frequency m_3 mode shows an asymmetric distribution, characterised by $\alpha_3 \approx 0.8$ and $\beta_3 \approx 0.6$.

The frequency of maximum loss of the m_1 mode, $f_{\max,m_1}$, progressively decreases upon cooling in the N phase, while its dielectric strength, $\Delta\varepsilon_{m_1}$, increases sharply. This mode is attributed to reorientations of the longitudinal component of the dipolar groups about the short molecular axis, analogous to the ω_1 relaxation predicted by the Nordio–Rigatti–Segre theory for uniaxial nematics composed of rigid dipolar molecules.[36] The observed decrease in $f_{\max,m_1}$ with decreasing temperature reflects the increasing orientational order and viscosity of the system.

However, two key features distinguish the m_1 process from the classical ω_1 relaxation of conventional nematogens. First, the dielectric strength increases dramatically upon cooling, reaching values of $\Delta\varepsilon_{m_1} \approx 2000$ near the M–N_F phase transition. Second, while $f_{\max,m_1}$ follows Arrhenius temperature dependence – as expected for this type of molecular reorientation – the associated activation energy is significantly higher, with $E_{A,m_1} \approx 170$ kJ mol^{-1}. This value is nearly twice than reported for similar reorientations in conventional nematogens,[35] and substantially higher than that observed for the corresponding process in DIO.[33]

Within the antiferroelectric M phase, and upon approaching the N_F transition, the m_1 mode exhibits soft-mode-like behaviour—characterised by a strong reduction in $f_{\max,m_1}$ accompanied by a divergent increase in dielectric strength. This trend is consistent with observations in DIO for the analogous relaxation mode.[33]

These findings suggest that the effective mean squared dipole moment along the nematic director is strongly influenced by short-range orientational dipolar correlations, quantified by the Kirkwood correlation factor g_1.[37,38] Although these correlations are short-ranged, they must be considered to rationalise both the magnitude and temperature dependence of the dielectric permittivity—particularly in anisotropic polar fluids—as recently demonstrated in the case of dimeric liquid crystals.[39]

Interestingly, weaker collective dipolar reorientations have also been reported in the nematic phase of the non-N_F-forming material RM734-CN.[40] In the present system, the pronounced reduction of $f_{\max,m_1}$, accompanied by a sharp increase in $\Delta\varepsilon_{m_1}$, can be attributed to collective fluctuations of dipolar clusters of molecules with parallel mutual alignment along the nematic director.

The deviation of the m_1 mode from Arrhenius behaviour in the M phase – marked by a critical slowing down of $f_{\max,m_1}$ – further suggests that the strength and extent of these dipolar correlations increase significantly in the intermediate antiferroelectric phase. These correlations appear to grow continuously until they become long-ranged at the transition to the N_F phase.

A few degrees below the isotropic–N transition, the contribution of the intermediate m_2 relaxation process was deconvoluted through simultaneous fitting of the real and imaginary parts of the dielectric permittivity, along with assessment of the fit quality in the derivative $d(\varepsilon')/d(\log f)$ (see Fig. S1). Notably, this represents the first time that the relaxation dynamics of the m_2 process have been deconvoluted across nearly the entire temperature range of the nematic phase. In contrast, the analogous low- and intermediate-frequency processes in DIO[10,33,41] and RM734[8,40] typically exhibit strong spectral overlap deep into the N phase. The clear time-scale separation between m_2 and m_1 in the present system is likely facilitated by the higher activation energy of the latter.

As shown in Fig. 5a, the relaxation frequency maximum of the m_2 mode follows an Arrhenius temperature dependence in the N phase, with an activation energy of $E_{A,m_2} \approx 110$ kJ mol^{-1}. The corresponding dielectric strength, $\Delta\varepsilon_{m_2}$, increases upon cooling but remains nearly two orders of magnitude lower than $\Delta\varepsilon_{m_1}$ (Fig. 5b). As the system approaches the M–N_F phase transition, the growth of polar order appears to influence the m_2 process, as evidenced by the increase in $\Delta\varepsilon_{m_2}$, while the softening of its relaxation frequency was also observed in DIO.[33]

These findings suggest that the m_2 process may be associated with individual dipolar reorientations, at least at higher temperatures within the N phase. Upon cooling, a clear time-scale separation emerges between the slower collective dipolar fluctuations of the m_1 mode and the faster, more localised motions of m_2, possibly occurring within dipolar clusters. Based on the observed activation energy and growing dielectric strength, the m_2 mode may involve reorientation of dipoles about the short molecular axis. However, this interpretation is somewhat counterintuitive, as the relaxation frequency does not slow significantly near the transition, suggesting that some form of precessional or hindered rotational motion may also be involved.

Yadav *et al.*[41] proposed that the intermediate mode in the high-temperature nematic phase of DIO is collective in nature, originating from the segregation of chiral conformers into domains with the same sense of chirality, with correlation lengths increasing upon cooling. The precise origin of the m_2 mode in the present system remains unclear and warrants further investigation, which is beyond the scope of this work.

The m_3 mode, which is the weakest in terms of dielectric strength, is recorded in the high-frequency region of the spectra. This process remains nearly temperature independent up to the middle of the N phase ($E_{A,m_3} \approx 12$ kJ mol^{-1}), while a slow reduction of the relaxation frequency is observed on further cooling. Based on the magnitude and the temperature dependence of its dielectric strength this process can be assigned to individual fluctuations of the projections of the

dipolar groups around the long molecular axis. This is also in line with the weak temperature variation of the relaxation time, as such motions are not hindered by the nematic potential. These trends are in agreement with those reported both for RM734[8,40] and DIO.[33]

Concerning the N_F phase, two relaxation mechanisms are recorded denoted as $N_{F,L}$ and $N_{F,H}$ following the notation proposed by Erkoreka *et al.*,[33,42] for the low- and high-frequency processes recorded in UUQU-4-N and DIO. The $N_{F,L}$ mode, a nearly Debye-type process located around 1 kHz, is distinguished by the huge and relatively temperature-independent dielectric strength in the order of 10^4. This process can be identified as a Goldstone (phason) mode according to Vaupotič *et al.*,[13] due to coupled fluctuations of director and polarisation or as a polarisation-external capacitance-goldstone (PCG) mode proposed by Clark *et al.*[11] The relaxation frequency of $N_{F,L}$ exhibits a negligible temperature dependence close the transition, while on further cooling below room temperature the reduction of the relaxation frequency is due to the increase in material viscosity. The high frequency mode $N_{F,H}$ exhibits a Havriliak–Negami shape with a relatively small strength and a slowly decreasing relaxation frequency. This process could be assigned to molecular reorientations around the long molecular axis, *i.e.* the evolution of the m_3 mode in the N_F phase. Another possibility is that $N_{F,H}$ corresponds to the high frequency phason mode predicted by the continuous phenomenological model of Vaupotič *et al.*[13]

However, in light of recent studies concerning the interpretation of the dielectric properties of ferroelectric nematogens, a rather unanimous conclusion is that the giant capacitance values measured in the N_F phase are apparent. The way that these apparent values are connected to the intrinsic material properties, *i.e.* the capacitance and resistance of the N_F layer, depends on the exact choice of the equivalent circuit for analysing the dielectric spectra. Clark *et al.*[11] have suggested that the block reorientation of spontaneous polarisation renders the N_F phase effectively conductive. This way the measured capacitance corresponds to the capacitance of the interfacial layers between the electrodes and the bulk material, either the polyimide insulating layers or the thin layers of the material itself. On the other hand, Matko *et al.*[34] and Vaupotič *et al.*[43] proposed the "high-ε" model, arguing that the analysis of the complete equivalent circuit in both bare and treated electrodes results in a resistivity of the N_F layer being of a similar magnitude to conventional nematogens and that the capacitance of the N_F phase is even higher than the measured apparent values. While the analysis of dielectric spectra through an appropriate equivalent circuit is of significant interest, it falls outside the scope of this study.

3.4. Mechanical properties

Reorientation of the uniformly aligned nematic director in a sandwich cell under a magnetic field is governed by the balance between magnetic and elastic torques. When the applied magnetic field exceeds a threshold value, the initially undisturbed director orientation becomes unstable—a phenomenon known as the magnetic Fréedericksz transition (mFT).[1,2] An analogous effect occurs under an electric field, termed the electric Fréedericksz transition (eFT), where a dielectric torque acts upon the director.

In both cases, the critical fields $B_c = \pi \Big/ d\sqrt{\mu_0 K_i/\chi_{m,a}}$ and $E_c = \pi \Big/ d\sqrt{K_i/\varepsilon_0\chi_{e,a}}$ are determined by the Frank elastic constants K_i and the corresponding anisotropies: diamagnetic ($\chi_{m,a}$) for mFT, and dielectric ($\chi_{e,a}$) for eFT. Therefore, measurements of the Fréedericksz threshold fields offer a reliable method for extracting the Frank elastic constants in nematic systems.

Magnetic Fréedericksz transitions are generally more straightforward to interpret, as magnetic fields do not couple directly to electric charges in the material, eliminating the influence of conductivity and the flexoelectric polarisation.[26] The splay transition is induced when a magnetic field is applied perpendicular to the substrate in a homogeneously aligned nematic cell, while a twist transition is observed when the field is applied parallel to the substrate and perpendicular to the undisturbed director (Fig. 6). A limitation of magnetic field measurements, however, is the need for accurate knowledge of the diamagnetic anisotropy, which is often challenging to determine directly.

In this study, we first determined the dielectric permittivity in the N phase as a function of the applied AC voltage across the cell. The recalculated $\varepsilon_{LC}(U)$ curves were fitted using Deuling's solution[28] for the director equilibrium equations, with a representative example depicted in Fig. 7. The threshold voltage obtained in the N phase is in the order of U_c = 0.1V, much smaller than in conventional nematics, and decreases upon cooling (see Fig. S2a). The dielectric permittivity ε_{LC} saturates at high fields, allowing the determination of the dielectric anisotropy through Deuling fitting. Although, the effect of the PI layers is discussed in the literature with respect to their effect on the measured permittivity in the N_F phase, we find that due to the high dielectric anisotropy of the N phase, the $\varepsilon_{LC}(U)$ can be significantly underestimated unless the contribution of the PI layers to the total measured sample capacitance is taken into account (see Fig. S3). This is especially important when measurements are conducted in thin cells with an increased d_{PI}/d ratio, that would result in an effective reduction of the measured permittivity and, consequently, of the calculated splay elastic constant with decreasing the sample thickness. Regarding the fitting process, Deuling's solution is valid sufficiently

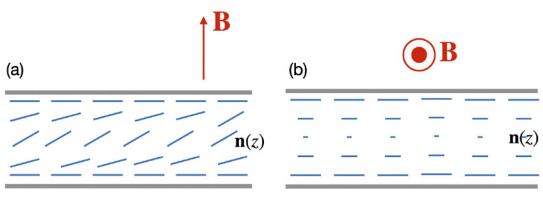

Fig. 6 Schematic representation of the measurement geometries for the splay (a) and twist (b) elastic constants using the magnetic Fréedericksz transition. **n** and **B** are the nematic director and the magnetic field, respectively. Strong planar anchoring condition is assumed.

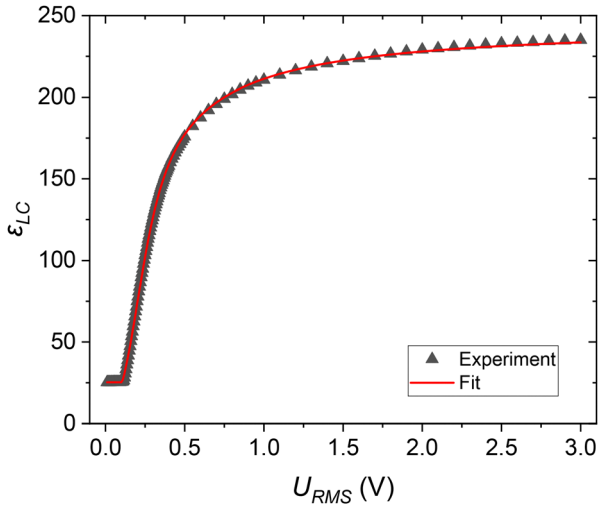

Fig. 7 Voltage dependence of the dielectric permittivity of the LC layer measured in the N phase at T = 78.5 °C and f = 1.5 kHz. The solid line represents the fit using eqn (3) and (4) with fitting parameters: U_{th} = 0.105 V, γ = 8.678, κ = 2.03 (K_{11} = 2.18 pN, K_{33} = 6.62 pN).

far from the nematic–modulated (N–M) phase transition (Fig. 7). Closer to the transition, significant deviations of $\varepsilon_{LC}(U)$ from the model suggest an increasing role of flexoelectric coupling between the director and the electric field. Near the transition to the M phase, only the splay elastic constant could be reliably estimated from the threshold voltage.

The dielectric anisotropy ($\chi_{e,a}$) extracted through eFT studies in the high-temperature nematic phase is presented in Fig. 8a. $\chi_{e,a}$ increases markedly on cooling, exceeding the values obtained in conventional nematics by at least one order of magnitude. The determination of $\chi_{e,a}$ and threshold voltage (U_c) through eFT (Fig. S2a), along with the critical magnetic field strength (B_c) through mFT (Fig. S2b) at the same temperatures, allows for the estimation of the temperature dependence of the diamagnetic anisotropy $\chi_{m,a} = \varepsilon_0\mu_0\chi_{e,a}(U_c/dB_c)^2$, shown in Fig. 8b. A Haller-type fit was applied in the high-temperature nematic phase to extrapolate values of the diamagnetic anisotropy into the ferroelectric nematic (N_F) region (Fig. 8b):[31]

$$\chi_{m,a} = \chi_{m,a0}\left(1 - \frac{T}{T^*}\right)^{\beta}$$

where $\chi_{m,a0}$ and β are empirical constants and T^* is an extrapolated temperature. The obtained fitting parameters are $\chi_{m,a0} = (6 \pm 1) \times 10^{-6}$, $T^* = (359.8 \pm 0.3)$ K and $\beta = (0.40 \pm 0.06)$. The Haller-type behaviour of the orientational order parameter across the whole range of N and N_F phases was established by birefringence measurements.

The temperature dependencies of the splay (K_{11}), bend (K_{33}), and twist (K_{22}) elastic constants are shown in Fig. 9a and b. In the nematic phase, K_{11} exhibits a pronounced decrease with decreasing temperature, especially as the system approaches the transition to the modulated phase M. In contrast, both K_{22} and K_{33} increase significantly. Two key effects may explain this behaviour: First, the flexoelectric coupling becomes increasingly

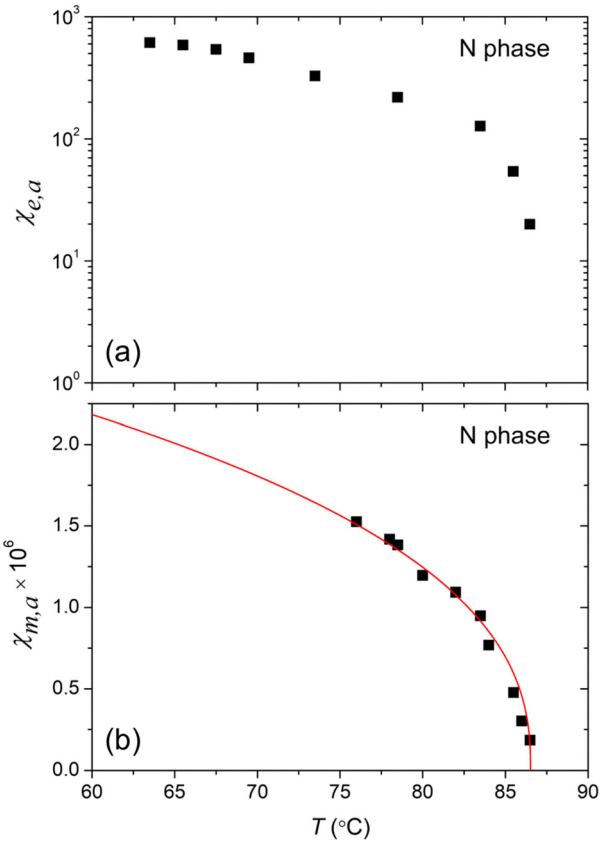

Fig. 8 Temperature dependences of (a) dielectric anisotropy ($\chi_{e,a}$) and (b) diamagnetic anisotropy ($\chi_{m,a}$) in the N phase. The red line represents the Haller fit.

important. The Landau–de Gennes (LdG) free energy for a ferroelectric nematic includes expansions in both the orientational order parameter Q and the polar order parameter P, containing various coupling terms.[7,44,45] The paraelectric–ferroelectric transition is primarily driven by terms involving powers of P. Notably, the term quadratic in P, with a temperature-dependent coefficient t, drives the system toward a ferroelectric state characterised by spontaneous splay deformation.[7,45] Even in the nematic phase ($t > 0$), this term, in combination with the flexoelectric coupling, leads to a reduction of the effective splay constant $K_{eff} = K_{11} - \frac{\gamma^2}{t}$, proportional to the square of the flexoelectric coefficient γ.

Second, the emergence of modulated, smectic-like order in the M phase suppresses bend elasticity, contributing to the increasing bend rigidity. In contrast, twist deformation remains largely unaffected, as the modulation wave-vector is orthogonal to the director.

In the N_F phase, the behaviour changes significantly. The splay elastic constant exhibits a sharp increase by nearly two orders of magnitude. As demonstrated in our previous work on an example of a compound with a single N_F phase, this enhancement is attributed to electrostatic contributions to the system's free energy.[26] The role of the electrostatic contributions have been discussed in various publications.[11,25,44,46] Splay deformations of the director generate bound charges

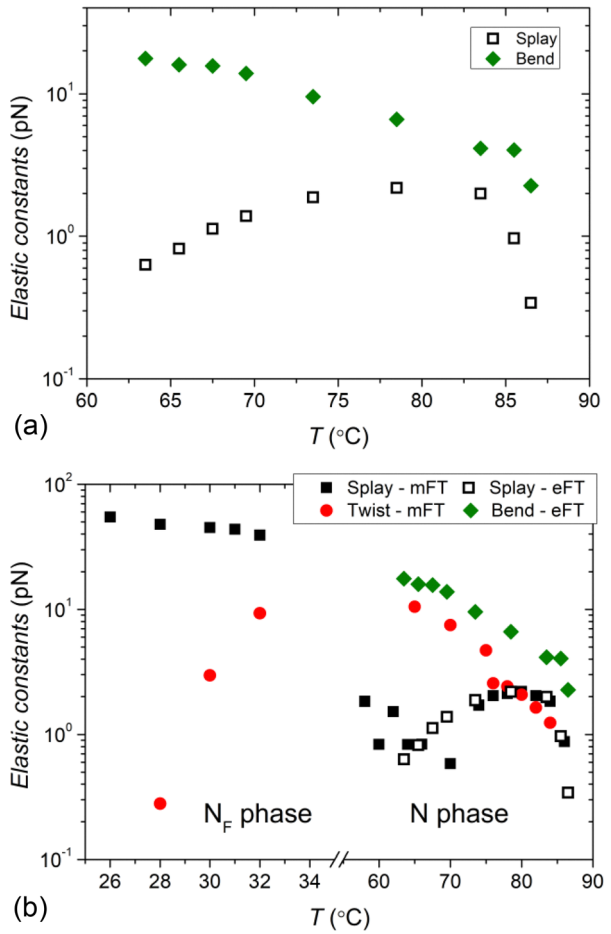

Fig. 9 Elastic constants in the N and N_F phases: (a) the splay (K_{11}) and bend (K_{33}) elastic constants in the N phase determined by eFT and fitting the dielectric permittivity $\varepsilon_{LC}(U)$ with eqn (3) and (4). (b) Comparison of the elastic constants determined using the mFT and eFT.

$\rho_b = -\nabla\cdot\mathbf{P}$, introducing an energetically unfavourable electrostatic component. The bound charges interact *via* screened electrostatic interactions, contributing the energy

$$U_{ES} = \frac{1}{8\pi\varepsilon\varepsilon_0}\int\int\frac{\rho(\mathbf{r})\rho(\mathbf{r}')e^{-\kappa|\mathbf{r}-\mathbf{r}'|}}{|\mathbf{r}-\mathbf{r}'|}d\mathbf{r}'d\mathbf{r}$$

where κ is the inverse Debye screening length[44] (see also S3 in ESI). Assuming that $\mathbf{P}(\mathbf{r}) = P_0\mathbf{n}(\mathbf{r})$, it is easy to show that splay elastic term has the same form as the electrostatic term yielding the effective splay elastic constant

$$K_{11}^{eff}(k) = K_{11} + \frac{P_0^2}{\varepsilon\varepsilon_0(k^2+\kappa^2)},$$

which is for the long wavelengths limit gives $K_{11}^{eff}(k) \approx K_{11} + P_0^2\lambda_D^2/(\varepsilon\varepsilon_0)$ with the Debye length $\lambda_D = 1/\kappa$. Substituting the typical values of P_0 = 6 μC cm^{-2}, bare liquid crystal dielectric permittivity ε = 100, and a typical Debye length of $\lambda_D \approx 100$ nm giving the correction 400 pN. Although this figure has a similar order of magnitude as observed in the experiment, the discrepancy can be attributed to the absence of the exact values for the bare dielectric constant and the Debye screening length.

The twist elastic constant exhibits significant softening in the N_F phase (Fig. 9b). The effect of the electrostatics on the twist elasticity is more complex. In an infinitely extended ferroelectric system, electrostatic interactions are not expected to renormalise the twist elastic constant. In bound systems, however, twist deformations can mitigate electrostatic interactions arising from dipole–dipole couplings and leading to twist instabilities.[47,48]

This twist instability may be understood as a result of competing elastic and electrostatic forces. In systems with degenerate anchoring, Coulomb interactions promote the formation of ambidextrous twist configurations, as predicted by Khachaturyan in ref. 47, studied by Lavrentovich *et al.*,[48] and experimentally demonstrated by Kumari *et al.*[49] in thin cells of DIO. Moreover, spontaneous chiral symmetry breaking was reported in polar nematic phase with heliconical structure.[21,50] Similar phenomena have been observed in other ferroelectric systems, such as bent-core nematics, where splay rigidity influences the formation of topological defects and inversion walls in freely suspended films. In the metastable uniform state, twist softening results from polarisation fluctuations, which become more suppressed at lower temperatures.

Ferroelectric nematics, with their true three-dimensional fluidity, offer a unique opportunity to study the interplay of elastic and electrostatic forces. This interplay gives rise to rich director field configurations, complex defect structures, and intriguing self-assembly behaviours under applied electric fields.

Conclusions

In conclusion, we have measured and compared the Frank elastic constants in a material exhibiting both paraelectric and ferroelectric nematic phases, primarily *via* magnetic Fréedericksz transition. Our findings confirm the softening of splay elasticity in the paraelectric phase and its subsequent hardening in the N_F phase, which we attribute to the electrostatic contributions arising from spontaneous polarisation. Softening of twist elasticity in the polar phase indicates Coulomb-driven twist instabilities and ambidextrous director configurations.

Author contributions

Evangelia E. Zavvou: conceptualisation, investigation, analysis, writing – original draft, writing – review and editing. Alexander Jarosik: investigation, analysis, review and editing. Hajnalka Nádasi: investigation, analysis, review and editing. Christoforos A. Krontiras: conceptualisation, review. Panagiota K. Karahaliou: conceptualisation, writing – review and editing. Rachel Tuffin: conceptualisation, materials resources, review. Melanie Klasen-Memmer: conceptualisation, materials resources, review. Alexey Eremin: conceptualisation, investigation, analysis, writing – original draft, writing – review and editing

Conflicts of interest

The authors declare the following financial interests/personal relationships which may be considered as potential competing interests: Alexey Eremin, Alexander Jarosik and Hajnalka Nádasi report financial support provided by German Research Foundation. Evangelia E. Zavvou reports financial support provided by the Hellenic Foundation for Research and Innovation.

Data availability

Data will be made available on request.

Supplementary information is available. See DOI: **https://doi.org/10.1039/d5sm00670h**.

Acknowledgements

We acknowledge the financial support of Deutsche Forschungsgemeinschaft (Projects NA1668/1-3 and ER 467/8-3). The authors thank Dr Nerea Sebastián and Dr Alenka Mertelj (Jožef Stefan Institute, Slovenia), Prof. Josu Martinez-Perdiguero (University of the Basque Country UPV/EHU, Spain) and Prof. Mikhail Osipov (University of Strathclyde, UK) for fruitful and motivating discussion. E. Z. acknowledges financial support from the Hellenic Foundation for Research and Innovation (HFRI PhD Fellowship grant, Fellowship Number: 809096).

References

1 P. G. d Gennes and J. Prost, *The Physics of Liquid Crystals*, Clarendon Press, 1995.
2 V. Fréedericksz and A. Repiewa, *Z. Phys.*, 1927, **42**, 532–546.
3 A. Mertelj, D. Lisjak, M. Drofenik and M. Čopič, *Nature*, 2013, **504**, 237–241.
4 M. Shuai, A. Klittnick, Y. Shen, G. P. Smith, M. R. Tuchband, C. Zhu, R. G. Petschek, A. Mertelj, D. Lisjak, M. Čopič and J. E. Maclennan, *Nat. Commun.*, 2016, **7**, 10394.
5 H. Nishikawa, K. Shiroshita, H. Higuchi, Y. Okumura, Y. Haseba, S. Yamamoto, K. Sago and H. Kikuchi, *Adv. Mater.*, 2017, **29**, 1702354.
6 R. J. Mandle, S. J. Cowling and J. W. Goodby, *Chem. – Eur. J.*, 2017, **23**, 14554–14562.
7 A. Mertelj, L. Cmok, N. Sebastián, R. J. Mandle, R. R. Parker, A. C. Whitwood, J. W. Goodby and M. Čopič, *Phys. Rev. X*, 2018, **8**, 041025.
8 N. Sebastián, L. Cmok, R. J. Mandle, M. R. de la Fuente, I. Drevenšek Olenik, M. Čopič and A. Mertelj, *Phys. Rev. Lett.*, 2020, **124**, 037801.
9 X. Chen, E. Korblova, D. Dong, X. Wei, R. Shao, L. Radzihovsky, M. A. Glaser, J. E. Maclennan, D. Bedrov, D. M. Walba and N. A. Clark, *Proc. Natl. Acad. Sci. U. S. A.*, 2020, **117**, 14021–14031.
10 S. Brown, E. Cruickshank, J. M. D. Storey, C. T. Imrie, D. Pociecha, M. Majewska, A. Makal and E. Gorecka, *Chem. Phys. Chem.*, 2021, **22**, 2506–2510.
11 N. A. Clark, X. Chen, J. E. MacLennan and M. A. Glaser, *Phys. Rev. Res.*, 2024, **6**, 013195.
12 A. Adaka, M. Rajabi, N. Haputhantrige, S. Sprunt, O. D. Lavrentovich and A. Jákli, *Phys. Rev. Lett.*, 2024, **133**, 038101.
13 N. Vaupotič, D. Pociecha, P. Rybak, J. Matraszek, M. Čepič, J. M. Wolska and E. Gorecka, *Liq. Cryst.*, 2023, **50**, 584–595.
14 A. Erkoreka, J. Martinez-Perdiguero, R. J. Mandle, A. Mertelj and N. Sebastián, *J. Mol. Liq.*, 2023, **387**, 122566.
15 P. M. Rupnik, L. Cmok, N. Sebastián and A. Mertelj, *Adv. Funct. Mater.*, 2024, **34**, 2402554.
16 A. Zattarin, E. Cruickshank, D. Pociecha, J. M. Storey, E. Gorecka and C. T. Imrie, *Liq. Cryst.*, 2024, **51**, 1035–1046.
17 M. Mrukiewicz, M. Czerwiński, N. Podoliak, D. Repček, P. Perkowski, R. J. Mandle and D. Węgłowska, *J. Mater. Chem. C*, 2024, **12**, 7214–7224.
18 X. Chen, V. Martinez, E. Korblova, G. Freychet, M. Zhernenkov, M. A. Glaser, C. Wang, C. Zhu, L. Radzihovsky, J. E. Maclennan, D. M. Walba and N. A. Clark, *Proc. Natl. Acad. Sci. U. S. A.*, 2023, **120**, e2217150120.
19 P. Medle Rupnik, E. Hanžel, M. Lovšin, N. Osterman, C. J. Gibb, R. J. Mandle, N. Sebastián and A. Mertelj, *Adv. Sci.*, 2025, **12**, 2414818.
20 H. Nishikawa and F. Araoka, *Adv. Mater.*, 2021, **33**, 2101305.
21 J. Karcz, J. Herman, N. Rychłowicz, P. Kula, E. Górecka, J. Szydlowska, P. W. Majewski and D. Pociecha, *Science*, 2024, **384**, 1096–1099.
22 C. J. Gibb, J. Hobbs, D. I. Nikolova, T. Raistrick, S. R. Berrow, A. Mertelj, N. Osterman, N. Sebastián, H. F. Gleeson and R. J. Mandle, *Nat. Commun.*, 2024, **15**, 5845.
23 P. Kumari, B. Basnet, H. Wang and O. D. Lavrentovich, *Nat. Commun.*, 2023, **14**, 748.
24 B. Basnet, M. Rajabi, H. Wang, P. Kumari, K. Thapa, S. Paul, M. O. Lavrentovich and O. D. Lavrentovich, *Nat. Commun.*, 2022, **13**, 3932.
25 F. Caimi, G. Nava, S. Fuschetto, L. Lucchetti, P. Paiè, R. Osellame, X. Chen, N. A. Clark, M. A. Glaser and T. Bellini, *Nat. Phys.*, 2023, **19**, 1658–1666.
26 E. Zavvou, M. Klasen-Memmer, A. Manabe, M. Bremer and A. Eremin, *Soft Matter*, 2022, **18**, 8804–8812.
27 A. Jarosik, H. Nádasi, M. Schwidder, A. Manabe, M. Bremer, M. Klasen-Memmer and A. Eremin, *Proc. Natl. Acad. Sci. U. S. A.*, 2024, **121**, e2313629121.
28 H. J. Deuling, *Mol. Cryst. Liq. Cryst.*, 1972, **19**, 123–131.
29 N. Sebastián, M. Čopič and A. Mertelj, *Phys. Rev. E*, 2022, **106**, 021001.
30 N. Sebastián, R. J. Mandle, A. Petelin, A. Eremin and A. Mertelj, *Liq. Cryst.*, 2021, **48**, 2055–2071.
31 I. Haller, *Prog. Solid State Chem.*, 1975, **10**, 103–118.
32 N. Yadav, Y. P. Panarin, W. Jiang, G. H. Mehl and J. K. Vij, *Phys. Chem. Chem. Phys.*, 2023, **25**, 9083–9091.
33 A. Erkoreka, A. Mertelj, M. Huang, S. Aya, N. Sebastián and J. Martinez-Perdiguero, *J. Chem. Phys.*, 2023, **159**, 159.

34 V. Matko, E. Gorecka, D. Pociecha, J. Matraszek and N. Vaupotič, *Phys. Rev. Res.*, 2024, **6**, L042017.
35 J. W. Goodby, P. J. Collings, T. Kato, C. Tschierske, H. Gleeson, P. Raynes and V. Vill, *Handbook of liquid crystals*, John Wiley & Sons, 2014, vol. 1.
36 P. Luigi Nordio, G. Rigatti and U. Segre, *Mol. Phys.*, 1973, **25**, 129–136.
37 J. G. Kirkwood, *J. Chem. Phys.*, 1939, **7**, 911–919.
38 P. Bordewijk, *Physica*, 1974, **75**, 146–156.
39 E. E. Zavvou, E. Ramou, Z. Ahmed, C. Welch, G. H. Mehl, A. G. Vanakaras and P. K. Karahaliou, *Soft Matter*, 2023, **19**, 9224–9238.
40 R. J. Mandle, N. Sebastián, J. Martinez-Perdiguero and A. Mertelj, *Nat. Commun.*, 2021, **12**, 4962.
41 N. Yadav, Y. P. Panarin, J. K. Vij, W. Jiang and G. H. Mehl, *J. Mol. Liq.*, 2023, **378**, 121570.
42 A. Erkoreka, N. Sebastián, A. Mertelj and J. Martinez-Perdiguero, *J. Mol. Liq.*, 2024, **407**, 125188.
43 N. Vaupotič, T. Krajnc, E. Gorecka, D. Pociecha and V. Matko, *Liq. Cryst.*, 2025, **2**, 1–13.
44 L. Paik and J. V. Selinger, *Phys. Rev. E*, 2025, **111**, L053402.
45 S. M. Shamid, S. Dhakal and J. V. Selinger, *Phys. Rev. E*, 2013, **87**, 052503–052512.
46 M. T. Máthé, N. Éber, Á. Buka, H. Nishikawa, F. Araoka, A. Jákli and P. Salamon, *J. Mol. Liq.*, 2025, **428**, 127525.
47 A. Khachaturyan, *J. Phys. Chem. Solids*, 1975, **36**, 1055–1061.
48 M. O. Lavrentovich, P. Kumari and O. D. Lavrentovich, *Nat. Commun.*, 2025, **16**, 6516.
49 P. Kumari, B. Basnet, M. O. Lavrentovich and O. D. Lavrentovich, *Science*, 2024, **383**, 1364–1368.
50 L. Lucchetti, *Science*, 2024, **384**, 1067–1068.

